ISABE-2015-20080

Numerical Investigation of Heat Transfer Effects on Internal Flow Dynamics of Micro Wave Rotor

Shi DENG[*†], Koji OKAMOTO[*], Kazuo YAMAGUCHI[**] and Susumu TERAMOTO[**]
[*]Department of Advanced Energy, Graduate School of Frontier Sciences, University of Tokyo
5-1-5 Kashiwanoha, Kashiwa-shi, Chiba, 277-8561, Japan
[**]Department of Aeronautics and Astronautics, School of Engineering, University of Tokyo

Abstract

Wave rotor is expected to increase the performance level of ultra-micro gas turbine when it is used as a topping cycle, nevertheless wave rotor itself may be affected by downsizing. Apart from the immediate effect of viscosity on the flow dynamics when the size reduces, the effects of heat transfer become more noticeable in small wave rotors. This work presents numerical investigations of heat transfer effects on the internal flow dynamics and consequently on the charging and discharging processes of wave rotor cells as the size reduces. A series of sizes scaled from a specified micro wave rotor is analyzed by three-dimensional numerical simulation. The results show that the initial state of compression process is much affected by heat transfer, which yields weaker shock waves in compression process and changes in charging and discharging of gas and air. According to the comparison between the results of different sizes, heat transfer effects on the charging and discharging processes grow significantly when the size is reduced from 1X size whose surface-area-to-volume ratio is 1.18 mm^{-1}. As regards heat transfer effects in small sizes of 1/3 and 1/10 (surface-area-to-volume ratio > 3.53 mm^{-1}), the change in charging and discharging conditions related to low pressure ports are the most noticeable. These considerable changes caused by heat transfer imply that much more attention to heat transfer effects is necessary for the design and investigation of such small wave rotors.

Nomenclature

A/V	Surface-area-to-volume ratio
D	Midspan diameter of wave rotor
D_H	Hydraulic diameter of cells
H	Height of cells
L	Axial length of cells
P	Pressure
q	Heat flux
q_m	Mass flow rate
r	Radial coordinate
T	Temperature
W	Width of cells
x	Axial coordinate
δ	Wall thickness
θ	Angular coordinate
Ω	Rotational speed

Subscript

0	Stagnation value
g	Gap
W	Width
w	Wall

[†]Graduated student

Introduction

Although small power systems like micro and ultra-micro gas turbines have attracted researchers over the last decades, it is difficult for such small gas turbines to achieve high cycle performance because of great losses (e.g. friction loss).[1-3] Wave rotor is a promising device that can enhance micro or ultra-micro gas turbine performance.

A wave rotor is a thermo-fluid device that directly exchanges energy between air and combustion gas by travelling pressure waves. Figure 1 shows a schematic arrangement of wave rotor components. Basically, a wave rotor consists of a series of cells (straight tubes) arranged around the shaft and several ports responsible for charging and discharging of fluids. Through rotation, cell ends open to the ports of different pressures alternately,

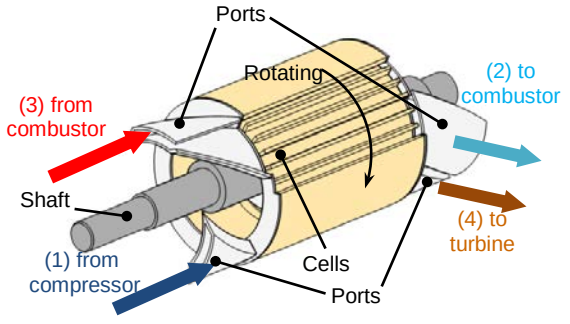

Fig. 1 Schematic arrangement of wave rotor components

and thereby pressure waves are generated and travel in the cells.

Wave rotor can be incorporated with an existing Brayton cycle system as a topping cycle component, as shown in Fig. 2. The maximum temperature and the total pressure ratio can be drastically enhanced, yielding higher turbine inlet pressure with the same turbine inlet temperature. This is an important feature especially for micro gas turbines, since the maximum temperature and overall pressure ratio are relatively low in small gas turbines.

Wave rotor cell is designed to open and close to the ports at definite timings to ensure that the internal flow field develops as expected. Figure 3 shows a schematic wave diagram, in which the characteristic lines of pressure waves and flows are depicted to represent the development of unsteady flow field in wave rotor cells. A full wave rotor cycle consists of compression and expansion processes.

Initially (θ = 0°: at the top in the figure), the cell is filled with low pressure fluid. As the cell moves downwards (θ ↑), its left end opens to Gas High pressure port (GH), and the primary shock wave is generated by the pressure difference between GH and the cell. This shock wave propagates rightwards, compresses the fluid initially in the cell, drives the rightwards fluid motion, and arrives at the right end. The shock wave is reflected at the right end and the reflected shock wave propagates leftwards, compressing the fluid in the cell again. At the same time of this shock wave reflection, the right end of the cell opens to Air High pressure port (AH), and the compressed fluid in the cell starts to flow into AH. When the reflected shock wave arrives at the left end, the left end shuts. This shutting causes a series of expansion waves by the inertia of inflow, which reduces the pressure in the cell. During opening to GH port, hot gas flows into the cell and the contact front (contact interface) between the hot gas and the fluid originally in the cell moves rightwards. The right end of the cell shuts when the expansion wave by the GH shutting arrives at the right end. As a result of this process, the fluid initially in the cell is compressed by the primary and reflected shock waves and it is completely scavenged into AH port. Then the compression process is finished.

Sequentially, the cell moves on and undergoes the expansion process. In this process, the right end opens to Gas Low pressure port (GL) to discharge the combustion gas, and an expansion wave is generated by the pressure difference between the cell and GL port. When this expansion wave arrives and reflects at the left end, the pressure in the cell becomes low enough and fresh air flows into the cell from Air Low pressure port (AL). A compression wave is generated by stopping the outflow with GL shutting, and AL shuts when this compression wave arrives at the left end.

In the cells, the working fluid inevitably exchanges heat energy with the lateral walls. Such heat exchange affects the temperature distribution in the cells, and consequently affects the whole wave

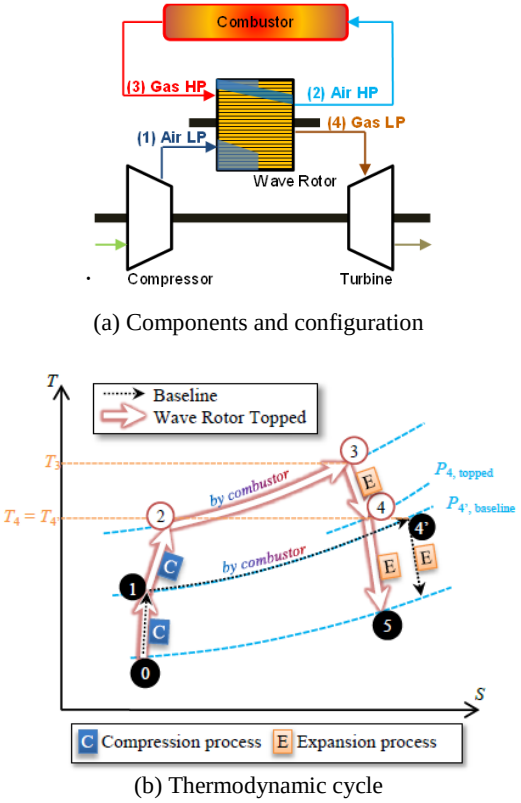

(a) Components and configuration

(b) Thermodynamic cycle

Fig. 2 Wave rotor topped gas turbine

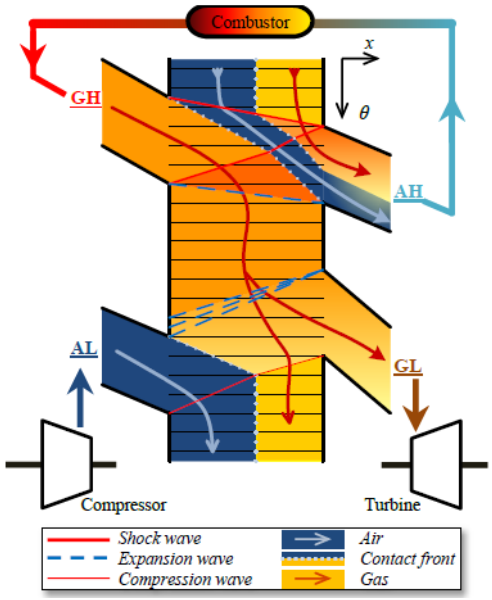

Fig. 3 Schematic wave diagram

diagram in Fig. 3.

In the past numerical researches, the lateral walls were mostly treated as adiabatic or in a steady-flow manner, and those treatments are applicable for wave rotors of conventional size. However, it is conceivable that the heat transfer effects on the internal flow dynamics become greater in smaller cells, owing to greater surface-area-to-volume ratio, as in the conventional turbo machineries, although the heat transfer effects in wave rotors have not been clarified yet in detail.[4-8]

Therefore, the objective of this study is to investigate numerically the heat transfer effects on the internal flow dynamics and resultant changes in the fluid charging and discharging in micro wave rotors. First, heat transfer effects on the internal flow dynamics are discussed by comparing the heat transfer case with the adiabatic case. Then, heat transfer effects in different sizes are compared and discussed to find out the trends of heat transfer effects as the size reduces.

Numerical Approach

In this study, a single rotating cell of wave rotor is considered, which consists of flow passage, solid wall and conjugate interface between cell fluid and solid wall (Fig. 4). The calculation region for fluid includes cell and clearance gap. The three-dimensional compressible Navier-Stokes equations with Baldwin-Lomax turbulence model are used to solve the flow passage, as shown in Table 1. This in-house code has been successfully developed and applied to a variety of steady and unsteady flows.[9-13]

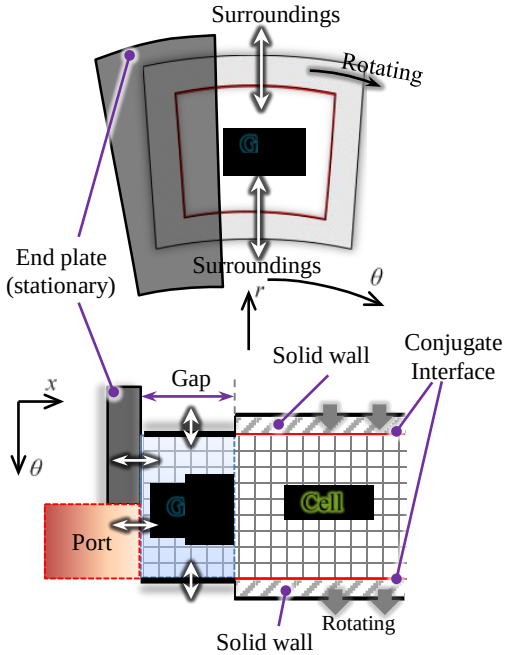

Fig. 4 Modeling of boundaries of flow passage

Three-dimensional unsteady heat conduction equation is also solved in the solid wall. The conjugate interface temperature is applied on both the lateral boundaries of flow passage and the internal surfaces of solid wall (Fig. 4). To calculate the conjugate interface temperature, the heat conduction in fluid as well as in solid has to be solved, and the heat conduction equation is modified to treat variable material properties.[14-15] This numerical scheme is consistent with that in the authors' previous study.[16]

The upper and lower sides of clearance gap region are connected to the surroundings, and the circumferential sides are treated as non-slip walls. The exact Riemann solver, which calculates the flux by Riemann invariance, is used to calculate inlet and outlet boundary conditions at the interface between the ports and calculation region.[4, 17] The temperature on the end faces of solid walls are fixed as 890 K, and the external surfaces of solid wall and stationary end plates are treated as adiabatic (Fig. 4).

Table 1 General description for fluid domain

Governing equations	3D Compressible N-S eq.
Flux splitting	SHUS & 3rd order MUSCL
Time stepping	LU-ADI with iterations
Turbulence modeling	Baldwin-Lomax

Ports

The ports shown in Fig. 5 are classified as charging ports on the left side and discharging ports

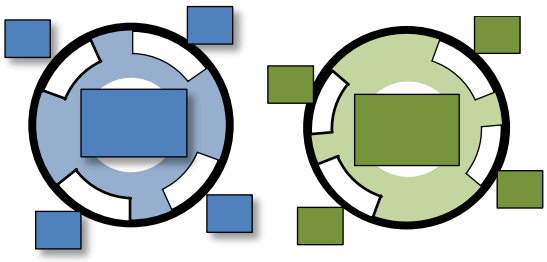

Fig. 5 Port configuration

Table 2 Starting degrees of opening and shutting

θ		Size		
		10X, 3X & 1X	1/3	1/10
GH	Open	0.00°	0.00°	0.00°
	Shut	50.0°	50.0°	49.0°
AL	Open	117°	117°	118°
	Shut	164°	166°	166°
AH	Open	21.6°	22.0°	21.6°
	Shut	66.0°	66.6°	66.0°
GL	Open	85.0°	81.0°	80.0°
	Shut	131°	128°	128°

on the right side. Every 180° finalize a wave rotor cycle. As the cell rotates clockwise around the axis, the left end of cell opens to GH and AL ports, and the right end opens to AH and GL ports, sequentially. The starting degrees of opening and shutting are listed in Table 2. Slight degree adjustments are applied when the size is reduced, in accordance with the flow field difference due to the effect of viscosity in downsized cells. These adjustments were calculated by the preliminary numerical simulation with adiabatic wall treatment.

The port conditions enumerated in Table 3 are assumed to be uniform and constant. The values are normalized by corresponding ones in AL port (total pressure of 0.30 MPa and total temperature of 440 K).

Table 3 Port conditions

		P_0	T_0
Charging side	GH	3.1	2.8
	AL	1.0	1.0
Discharging side	AH	3.4	2.1
	GL	1.2	2.2

Normalized by 0.30 MPa or 440 K

Wave Rotor Cell and Grid

Five different sizes scaled from the cell of a micro wave rotor, which is designed to be integrated into a micro gas turbine of 1-10 kW output,[9] are investigated to compare the heat transfer effects in different sizes. The geometry of cell is shown in Fig.

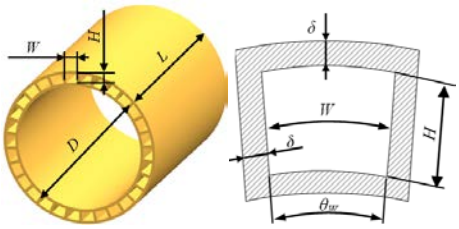

Fig. 6 Geometry of micro wave rotor cell

Table 4 Dimensions of micro wave rotor cell

	10X	3X	1X	1/3	1/10	Unit
D	470	141	47.0	15.7	4.70	mm
L	690	207	69.0	23.0	6.90	mm
W	39.2	11.8	3.92	1.31	0.392	mm
H	30.0	9.00	3.00	1.00	0.30	mm
θ_W	9.56	9.56	9.56	9.56	9.56	°
D_H	34.3	10.3	3.43	1.14	0.343	mm
δ	10.0	3.00	1.00	0.333	0.10	mm
x_g	1.00	0.30	0.10	0.0333	0.01	mm

Table 5 Rotation speed of cell (in RPM)

	10X	3X	1X	1/3	1/10
Ω	3,100	10,050	30,000	88,000	264,000

6 and the dimensions relating to the cells are shown in Table 4. As shown in this table, 10X, 3X, 1/3 and 1/10 are geometrically scaled from 1X of original one. The gap size (x_g) between cell and end plate (Fig. 4) is also specified in Table 4, and the rotation speed is specified in Table 5.

The three-dimensional orthogonal structured grid of fluid domain is shown in Fig. 7, and it has 201×101×101 grid points in x, r and θ directions. Ideal gas is used in the fluid domain. In the solid wall, from the conjugate interface to external surfaces, the depth coordinates of grid points are shown in Fig. 8; the grid spacing grows rapidly for the concern of great momentary heat flux near the interface. Stainless steel whose material properties are listed in Table 6 is used in the solid wall domain.

Verification of Conjugate Interface Temperature

Since the interface temperature is used as the boundary condition for both flow and solid domains, it is necessary to verify the numerical solution of the

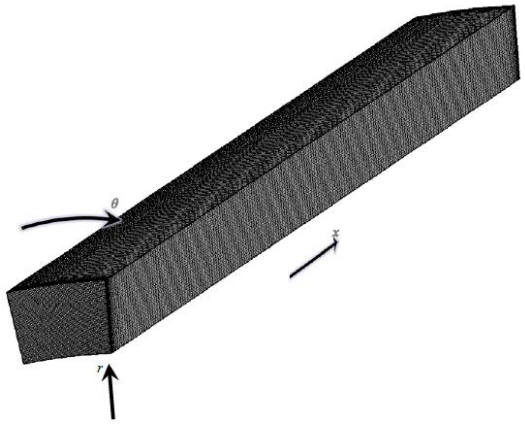

Fig. 7 Grid of fluid domain

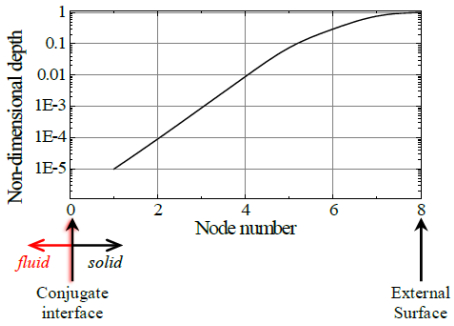

Fig. 8 Depth coordinates of grid points in wall (normalized by wall thickness δ)

Table 6 Material properties of solid

Parameter	Value	Unit
Thermal conductivity	25	W/(m·K)
Density	8,000	kg/m^3
Specific heat	500	J/(kg·K)

interface temperature by comparing with analytical solution. For verification, an infinite plate with initial temperature $T_{0,1}$, and the infinite medium with an initial temperature $T_{0,2} < T_{0,1}$ are considered. The plate is then cooled by heat conduction, and the time-dependent interface temperature can be obtained by the analytical solution,[18] as follows.

$$\Theta_{\text{intf}} = \frac{T_{\text{intf}} - T_{0,2}}{T_{0,1} - T_{0,2}} = \frac{K_\epsilon}{1+K_\epsilon} - \frac{2K_\epsilon}{1+K_\epsilon} \sum_{n=1}^{\infty} (-H)^{n-1} erfc\left(\frac{n\delta}{(\alpha_1 t)^{1/2}}\right) \quad (1)$$

Here, Θ is dimensionless temperature, subscript intf denotes interface. Further information related to the analytical solution can be found in the literature.[18]

The verification of interface temperature treatment in a relatively long period is fulfilled in order to understand the accumulative difference in a long run of numerical simulation of many wave rotor cycles that may be necessary before a periodic solution is obtained (for example, for 1X size wave rotor to be introduced in the next section, the time of a wave rotor cycle corresponds to the Fourier number, $Fo_1=4.4\times10^{-3}$). Since the density in the flow passage varies in wave rotor cell, the situations involving the smallest density and the greatest density are calculated and compared for verification. In both cases, the temperature distribution at $Fo_1=3.6\times10^{-2}$ (Fig. 9 (a)) or $Fo_1=0.18$ (Fig. 9 (b)) calculated by the analytical solution[18] is used as the initial field of numerical simulation. The differences of the interface temperature in analytical and numerical results are no more than 1×10^{-4}. Considering the possible temperature range (2.8-1.0) × 440 K = 792 K (see Table 3), the absolute temperature difference is $1\times10^{-4}\times$ 792 K < 0.1 K, a limited small difference.

In addition, considering that the thermal boundary layer is extremely thin behind a propagating shock wave, corresponding short-term response has been verified, and the differences between numerical and analytical results are confirmed to be negligible. As a result of both long-term and short-term verifications, the present numerical method of interface temperature is sufficient for the present research.

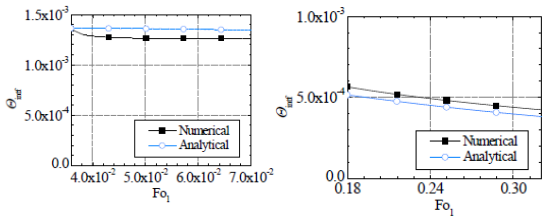

(a) Greatest density (b) Smallest density

Fig. 9 Time history of interface temperature

Results and Discussions

Heat Transfer Effects on Internal Wave Dynamics in 1/10 Size

When heat transfer is taken into account, periodicity of both internal flow and wall temperature are confirmed in all results (both L2 residual of flow field and maximum residual of wall temperature are less than 1e-5), so that the cyclic flow field, heat flux and wall temperature can be discussed. To address the heat transfer effects on internal wave dynamics, the results of adiabatic case and heat transfer case of 1/10 size are compared in this section as an example, because the greatest effects are observed in this size.

During a cycle, the wall temperature changes little (the oscillation amplitude is less than 0.01 in normalized temperature), and the axial distribution of wall temperature, which is the average of interface temperature on the four wall surfaces at each x-position, is shown in Fig. 10 for the moment of $\theta = 0°$ as a representative. The wall temperature falls in the range of 2.0~2.1. Compared with the temperatures of charging ports in Table 3, the wall temperature is close to the average temperature of charging ports.

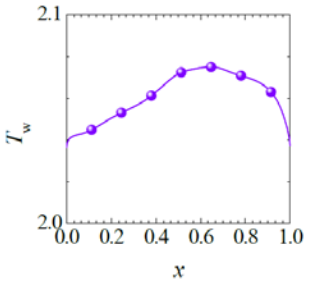

Fig. 10 Axial distribution of wall temperature (1/10 size, normalized by 440 K)

Figure 11 shows the distribution of heat flux in a wave rotor cycle from 0° to 180°, each point in the wave diagram denoting the average heat flux on the four wall surfaces at each axial position x and degree θ. Similar to the schematic wave diagram in Fig. 3, contact fronts, shock waves, compression waves and expansion waves are depicted on this wave diagram, and it is also divided into "air" and "gas" regions by contact fronts. As a consequence of T_w = 2.0~2.1, during opening to GH and AL, the hot gas from GH port loses much heat to wall (red zone near GH) and the cold air from AL port absorbs much heat from wall (blue zone near AL). Great heat flux (positively or negatively) is also found behind the pressure waves.

The wave diagram of total pressure of the heat transfer case is shown in Fig. 12. For specific and precise comparison between heat transfer case and

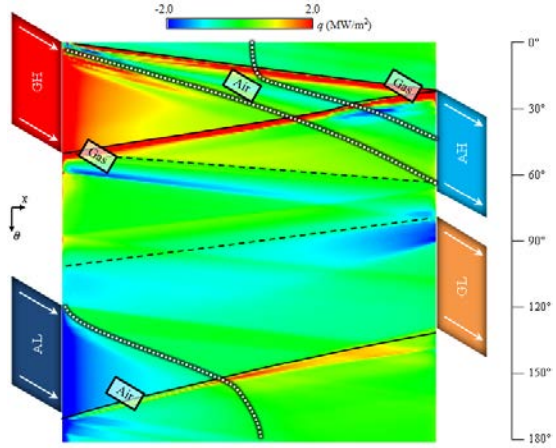

Fig. 11 Wave diagram colored in heat flux (1/10 size; ports only show their locations)

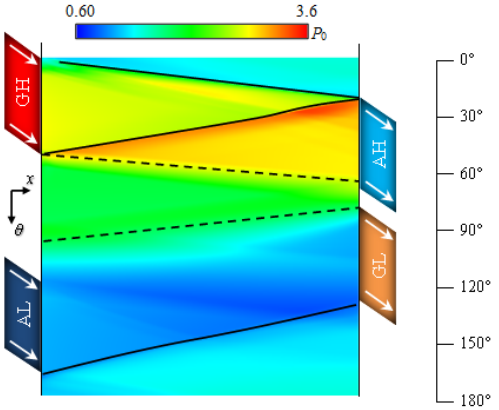

Fig. 12 Wave diagram colored in total pressure (1/10 size; ports only show their locations)

adiabatic case, axial distributions of total pressure at several degrees are selected and exhibited in Fig. 13. Because the cold air is persistently heated after being charged into the cells (blue zone to the left of contact front in bottom-left region of Fig. 11, about 120° ~ 180°), the total temperature of air at 0° (180°) is higher in the heat transfer case than that in the adiabatic case (Fig. 14), and the total pressure of air is also higher in the heat transfer case (Fig. 13 (a)) owing to such heating. However, the pressure difference is smaller than the temperature difference due to the leakage from the clearance gap.

The difference in the initial state at 0° leads to further differences in total pressure in the cells. Figure 13 (b) shows the axial distribution of total pressure when the primary shock wave (PSW) is propagating rightwards. The pressure ratio of PSW is smaller in the heat transfer case than in the adiabatic case, i.e. PSW is weaker in the heat transfer case. This is because the initial pressure in the cell is higher in the heat transfer case as mentioned above, while the pressure in GH is set as constant.

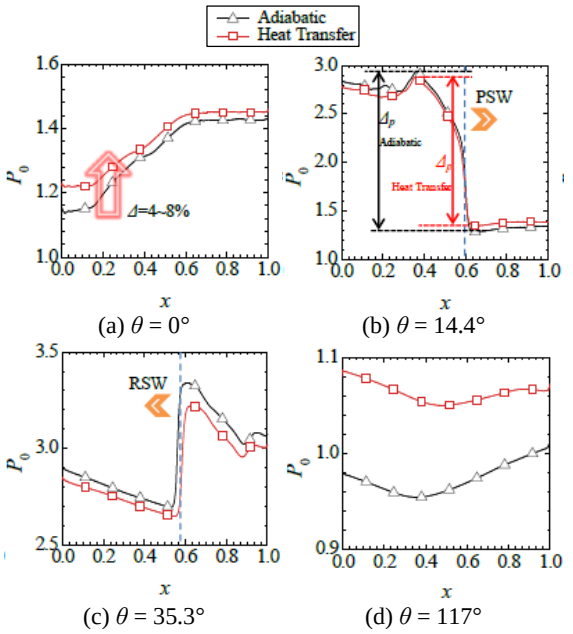

Fig. 13 Axial distributions of total pressure at selected degrees (1/10 size; PSW: primary shock wave; RSW: reflected shock wave)

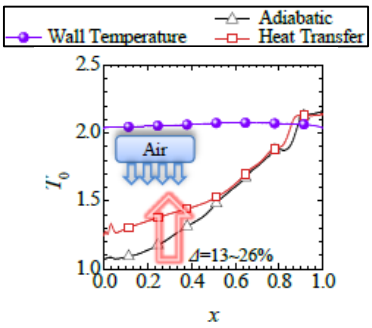

Fig. 14 Axial distributions of total temperature at θ = 0° (1/10 size)

Figure 13 (c) shows the pressure distribution when the reflected shock wave (RSW) is propagating leftwards, and RSW is also weaker in the heat transfer case. Besides, the total pressure of the fluid behind RSW, which relates to the pressure in AH port, is lower in the heat transfer case.

Furthermore, during the expansion process (80.0°~166°), the total pressure is higher in the heat transfer case (Fig. 13 (d)), which is caused by heating during opening to GL port (blue color in 80.0°~128° in Fig. 11), in addition to the pressure difference in the compression process.

Heat Transfer Effects on Charging and Discharging in 1/10 Size

Since the pressure waves are affected by heat transfer, the charging and discharging processes are

subject to change. Figure 15 shows the degree (i.e., time) history of the total pressure at a cell end during charging or discharging when it is exposed to a port. Due to the lower total pressure in the cell during the compression process (Fig. 13(b), (c)), the discharging total pressure to AH port is lower in the heat transfer case (Fig. 15 (a)). On the other hand, when the left end opens to AL port in the expansion process, the total pressure during charging becomes higher in the heat transfer case (Fig. 15 (b)).

To discuss the overall effect, the difference between adiabatic case and heat transfer case is calculated by

$$\Delta_a = Average\ in\ heat\ transfer - Average\ in\ adiabatic \quad (2)$$

The differences in total pressure $\Delta_a P_0$ during charging and discharging for corresponding ports are shown in Fig. 16. It is clear that the total pressure during compression process (opening to GH or AH) is lower in the heat transfer case, while it is higher during the expansion process (opening to AL or GL).

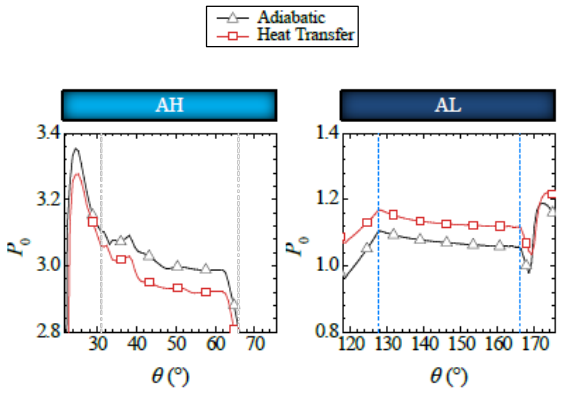

(a) For AH port (b) For AL port

Fig. 15 Degree history of total pressure at the right end of cell during opening to AH or AL ports (1/10 size)

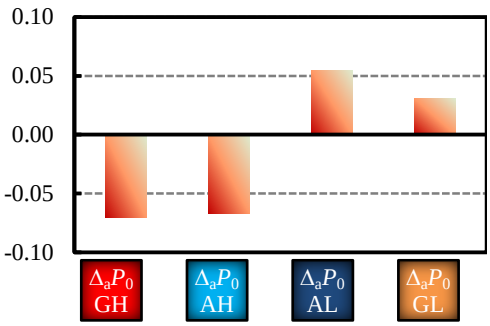

Fig. 16 Differences in average total pressure when opening to ports (1/10 size; normalized by P_0 of AL)

The differences in mass flow rate at the cell ends $\Delta_a q_m$ (Fig. 17) reveal that 1) charging from GH is enhanced because the pressure in cell is reduced whereas the state in the port is constant, and discharging to AH is lessened for the same reason; 2) charging from AL is decreased and discharging to GL is increased because the pressure in cell is increased whereas the state in port is constant.

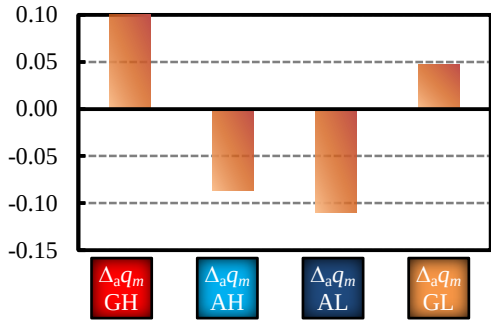

Fig. 17 Differences in mass flow rate when opening to ports (1/10 size; normalized by q_m of AL)

Heat Transfer Effects across Sizes

To find out the trend of heat transfer effects on the charging and discharging, relative differences (Eq. (3)) in total pressure and mass flow rate at cell ends for all the sizes investigated (10X, 3X, 1X, 1/3, and 1/10) are summarized in Fig. 18 and Fig. 19. To

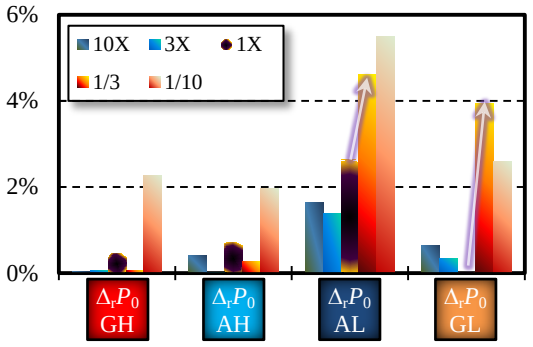

Fig. 18 Percentages of differences in average total pressure when opening to ports for various sizes

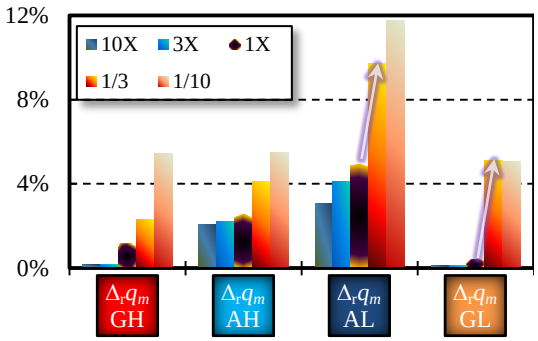

Fig. 19 Percentages of differences in mass flow rate when opening to ports for various sizes

understand the scale of the sizes, the surface-area-to-volume ratio is listed in Table 7 as a reference.

$$\Delta_r = \left| \frac{Average\ in\ heat\ transfer}{Average\ in\ adiabatic} - 1 \right| \qquad (3)$$

Table 7 Surface-area-to-volume ratio of all sizes investigated (in mm^{-1})

	10X	3X	1X	1/3	1/10
A/V	1.18×10^{-1}	3.53×10^{-1}	1.18×10^{0}	3.53×10^{0}	1.18×10^{1}

In regard to the differences in total pressure $\Delta_r P_0$ (Fig. 18), the difference rises dramatically from 1X size to 1/3 size during opening to low pressure ports AL and GL. Besides, for the total pressure during opening to low pressure ports AL and GL, $\Delta_r P_0$ is relatively notable in 1/3 and 1/10 size compared with those in larger sizes. Concerning the difference in mass flow rate $\Delta_r q_m$ (Fig. 19) related to the low pressure ports AL and GL, drastic increase is also found from 1X size to 1/3 size, and relatively noteworthy ones also occurs in 1/3 size and 1/10 size.

Hence, it can be inferred that the heat transfer effects in sizes smaller than 1X size, i.e. the size whose surface-area-to-volume ratios is greater than 1.18 mm^{-1}, would require much more attention.

Conclusions

In the present study, numerical simulations are carried out for wave rotors of various size in order to investigate heat transfer effects in micro wave rotor, and the following conclusions were obtained.

1) The fresh air is heated after being charged into the cells, and consequently the total pressure and total temperature in the cells before compression process are raised by heat transfer. This causes further changes in the internal flow dynamics and charging / discharging of gas and air.

2) When the size is reduced from 1X size (i.e., surface-area-to-volume ratio is larger than 1.18 mm^{-1}), heat transfer effects on charging and discharging related to low pressure ports (AL and GL) grow drastically. Especially, when the surface-area-to-volume ratio is larger than 3.53 mm^{-1}, those heat transfer effects become so significant, therefore much more attention to the heat transfer effects is necessary for the design and investigation of such small wave rotors.

References

[1] A. H. Epstein, et al., "Micro-Heat Engines, Gas Turbines and Rocket Engines," AIAA-97-1773, 1997.

[2] A. H. Epstein, "Millimeter-Scale, MEMS Gas Turbine Engines," in ASME Turbo Expo 2003, pp. 669–696.

[3] K. Okamoto, T. Nagashima, and K. Yamaguchi, "Design and Performance of a Micro Wave Rotor," 17th International Symposium on Airbreathing Engines, ISABE-2005-1270, 2005.

[4] K. Okamoto and T. Nagashima, "Simple Numerical Modeling for Gasdynamic Design of Wave Rotors," Journal of Propulsion and Power, 23(1), pp. 99–107, 2007.

[5] K. J. Elloye and J. Piechna, "Influence of the Heat Transfer on the Operation of the Pressure Wave Supercharger," Archive of Mechanical Engineering, XLVI(4), pp. 297–309, 1999.

[6] D. E. Paxson and J. Wilson, "Recent improvements to and validation of the one dimensional NASA wave rotor model," NASA TM-106913, May 1995.

[7] H. E. Weber, "Shock Wave Engine Design," John Wiley & Sons, New York, USA, 1995, pp. 121–126.

[8] L. Pohořelský, P. Sané, T. Rozsas, and N. Müller, "Wave Rotor Design Procedure for Gas Turbine Enhancement," in ASME Turbo Expo 2008: Power for Land, Sea, and Air, 2008, pp. 847–860.

[9] K. Fujii and S. Obayashi, "Navier-Stokes simulations of transonic flows over a practical wing configuration," AIAA journal, 25(3), pp. 369–370, 1987.

[10] K. Fujii and S. Obayashi, "High-resolution upwind scheme for vortical-flow simulations," Journal of Aircraft, 26(12), pp. 1123–1129, 1989.

[11] T. Ogawa and K. Fujii, "Numerical investigation of three-dimensional compressible flows induced by a train moving into a tunnel," Computers & Fluids, 26(6), pp. 565–585, 1997.

[12] S. Teramoto, K. Hiraki, and K. Fujii, "Numerical analysis of dynamic stability of a reentry capsule at transonic speeds," AIAA journal, 39(4), pp. 646–653, 2001.

[13] K. Isomura, M. Murayama, S. Teramoto, K. Hikichi, Y. Endo, S. Togo, and S. Tanaka, "Experimental verification of the feasibility of a 100 W class micro-scale gas turbine at an impeller diameter of 10 mm," Journal of micromechanics and microengineering, 16(9), pp. S254, 2006.

[14] S. V. Patankar, "Numerical Heat Transfer and Fluid Flow," McGraw-Hill, New York, USA, 1980, pp. 60–102.

[15] J. C. Jo, Y. H. Choi, and S. K. Choi, Numerical analysis of unsteady conjugate heat transfer and thermal stress for a curved piping system subjected to thermal stratification, Journal of Pressure Vessel Technology, 125 (4), pp. 467–474, 2003.

[16] S. Deng, K. Okamoto and S. Teramoto, "Numerical investigation of heat transfer effects in small wave rotor," Journal of Mechanical Science and Technology, 29(3): 939–950, 2015.

[17] E. F. Toro, "Riemann Solvers and Numerical Methods for Fluid Dynamics," Springer, New York, USA, 1997, pp. 115–151.

[18] A. V. Luikov, "Analytical Heat diffusion theory," Academic Press, New York, USA, 1968, pp. 238–240.